ACS APPLIED NANO MATERIALS

www.acsanm.org Article

Scalable Drop-to-Film Condensation on a Nanostructured Hierarchical Surface for Enhanced Humidity Harvesting

Ankit Nagar, Ramesh Kumar, Pillalamarri Srikrishnarka, Tiju Thomas,* and Thalappil Pradeep*

Cite This: *ACS Appl. Nano Mater.* 2021, 4, 1540−1550 Read Online

ACCESS | Metrics & More | Article Recommendations | Supporting Information

ABSTRACT: Active cooling-based atmospheric water generators, despite their growing demand, continue to be energy intensive and offer poor collection efficiencies (energy consumption per liter of water production). Despite progress in micro-/ nanofabrication techniques and functional coatings, advanced surfaces have not been successfully scaled onto such harvesters to accelerate condensation and improve their efficiencies. Here, we present a scalable dual-nanostructured hierarchical surface that comprises sporadically distributed bundles of randomly oriented faceted microcones having facets composed of nanostructures, which are either bumps or ridges. Condensate removal on this surface occurs via drop-to-film coalescence, followed by film shedding in the form of macrodrops. Compared to a conventional plain metal surface used for condensation, the improvement in latent heat transfer coefficient using a hierarchically textured surface ranged from 19.9% at a subcooling of ∼8 °C to 1048.4% at a subcooling of ∼1 °C in laboratory scale experiments, subcooling being defined with respect to the dew point. To demonstrate utility at industrial scale and to ensure scalability of the modified surfaces, we create a prototype assembly comprising a tube-fin heat exchanger with hierarchically textured fins, cooled using a standard refrigeration cycle, producing ∼25 L of water per day. The prototype containing hierarchically textured fins provides ∼10.8% enhanced water collection at ∼10.4% improved average collection efficiency compared to the traditional water generator when tested in outdoor conditions.

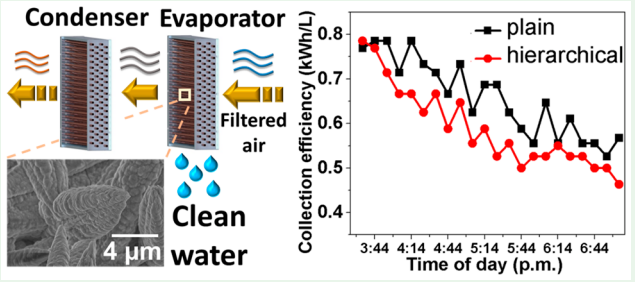

KEYWORDS: *condensation, heat transfer, hierarchical nanostructures, water harvesting, drinking water*

INTRODUCTION

Atmospheric water generators (AWGs) have gained significant scientific and commercial attention in the past decade because of their ability to provide clean water in regions of extreme water scarcity.[1] Most of the commercial AWGs are based on a refrigeration cycle, where a coolant undergoes a reverse Carnot cycle to exchange heat with the surrounding air and enable its condensation.

The collection efficiency of such an AWG system can be defined as energy consumption per unit volume of product water. It depends on ambient temperature and humidity. Although efficiencies of current AWGs are improved by implementing varied configurations of heat exchangers to extend the air−surface contact time,[2] hydrophobizing the copper tubes to promote jumping-droplet condensation,[3] or preconcentrating moisture in the input air to increase the dew point temperature,[4] the fin surfaces of heat exchangers have rarely been modified to enhance the overall performance.[5] In this work, we present rationally designed hierarchical structures created on aluminum fins of heat exchangers, prepared using a one-step, top-down process, in which condensed droplets drain by combining with the liquid film present on the surface. Subsequently, the film sheds itself under gravity, in the form of macrodrops. Such a mechanism of shedding is then compared with the already existing mechanisms of dropwise (DwC),[6−10] filmwise (FwC),[11−13] and state-of-the-art hierarchical condensation, by choosing the appropriate test surfaces that are known to demonstrate these mechanisms.[14,15] We perform lab-scale water collection experiments across the entire possible range of subcooling (∼0−8 °C, below the dewpoint), on chosen test surfaces to compare their water harvesting abilities. As a final step, we build a prototype atmospheric water generator (AWG) comprising of hierarchically textured surface for condensation and compare it against an identical counterpart (representative of a conventional AWG) having plain metal surface for condensation. The results show an ∼10.4% improvement in the collection efficiency, and an ∼10.8% improvement in the overall water collection.

Received: November 12, 2020
Accepted: February 5, 2021
Published: February 18, 2021

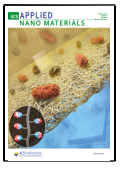

https://dx.doi.org/10.1021/acsanm.0c03032
ACS Appl. Nano Mater. 2021, 4, 1540−1550

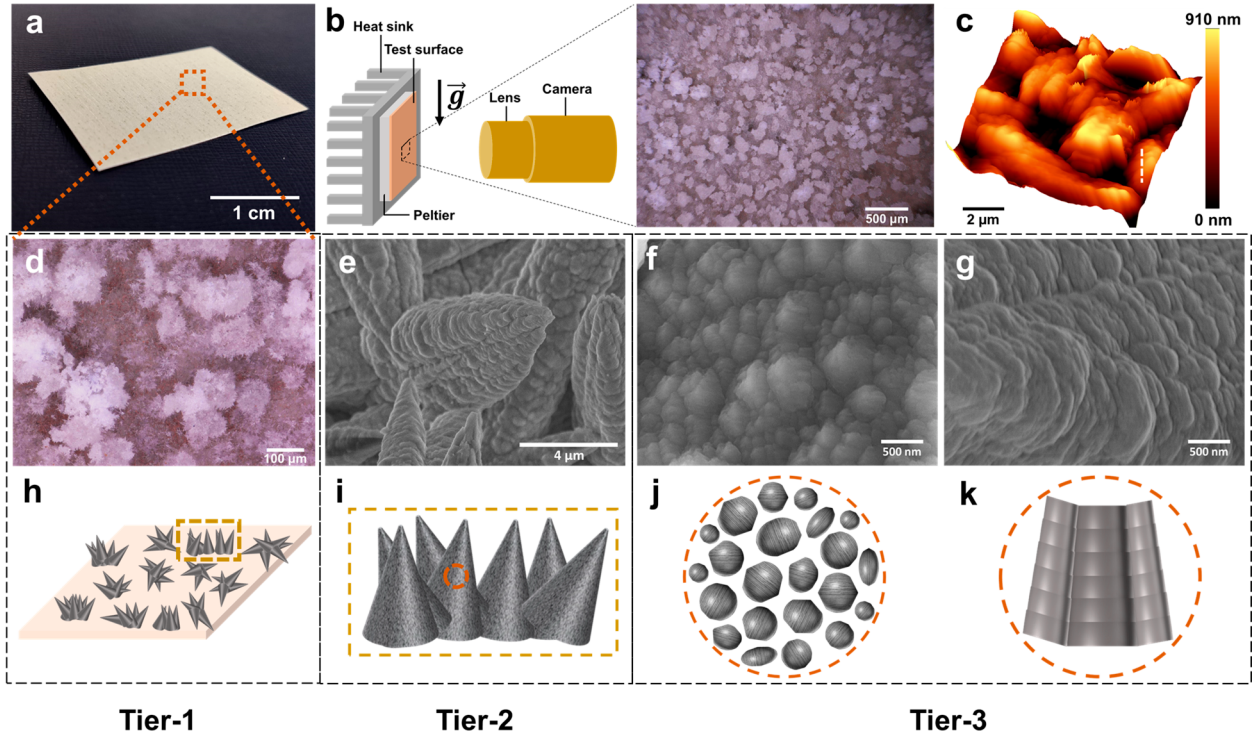

Figure 1. Hierarchical surface. (a) Photograph of the hierarchical surface. (b) Setup for optical microscopy (not to scale). (c) AFM topography image of the surface showing height variation, and dashed white line indicating chosen linear path for measuring average nanoscale (tier-3) roughness. (d) Optical image of the surface showing bundles. (e) FESEM image of a few faceted microcones of a bundle in random orientation. (f) FESEM image showing facet of a cone with presence of irregularly shaped nanobumps, and nanochannels dividing the bumps. (g) FESEM image of another conical facet possessing parallel ridges divided by nanochannels. (h–k) Respective schematics of the surface showing bundles as tier-1 of the hierarchy, faceted microcones as tier-2, and the dual nanostructures as tier-3.

Scheme 1. Plain Aluminum Surface (p) Functionalized with 1H, 1H, 2H, 2H-Perfluorodecyltriethoxysilane (PDES) to Achieve a Plain Hydrophobic Surface (p-hp) and Plain Surface Etched to Create a Hierarchical Surface (h), Which was Silanized by PDES to Result in a Hierarchical Hydrophobic Surface (h-hp)[a]

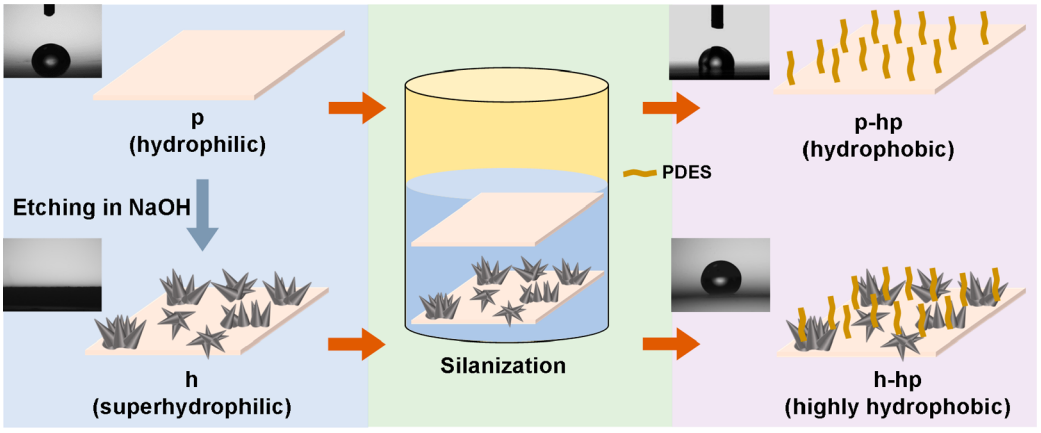

[a]The respective static contact angle measurements are shown in the insets and contact angle data are shown in Table 1.

RESULTS AND DISCUSSION

Dual-Nanostructured Hierarchical Surface. A lower radius of curvature of a nucleation site results in a faster rate of vapor diffusion.[16] Thus, quicker droplet growth occurs selectively on "pointed" sites. Therefore, we propose a surface design comprising sharp micrometer-sized structures and additional nanostructures on top of these microstructures to promote nucleation more effectively.

Sophisticated techniques like photolithography[10,17] and deep reactive-ion etching[18] are multistep and expensive. In addition, prospects for scalability are a concern. In contrast, we use a simple, one-step chemical etching approach to create the hierarchical surface.

In Figure 1, we present the hierarchical structures created on an aluminum sheet via the etching process. A photograph of the sheet postetching is shown in Figure 1a. The top level of hierarchy (tier-1) was observed through optical microscopy (setup shown in Figure 1b) and comprises bundles in the range of 100 μm, as shown in Figure 1d. Other than the regions covered with bundles, the surface also has white

https://dx.doi.org/10.1021/acsanm.0c03032
ACS Appl. Nano Mater. 2021, 4, 1540–1550

regions at the base, as visible in Figure 1d. As observed in FESEM, all bundles as well as white regions at the base comprise randomly oriented faceted microcones (tier-2), as shown in Figure 1e. The facets of these cones comprise two types of morphologies, nanobumps and parallel nanoridges, all of which vary in size and shape, as shown in Figure 1g and h, respectively. These together constitute tier-3 of the hierarchy. Pictorial representations of the surface are shown in Figures 1h−-k. Average surface roughness constituted by the entire hierarchy was measured as 212.9 nm, obtained using atomic force microscopy (Figure 1c). Average nanoscale roughness comprising the tier-3 nanostructures present on the surface of microcones was linearly measured on one of the conical surfaces and was obtained as 19.3 nm (dashed white line in Figure 1c). More details are discussed in the Methods section.

Choice of Test Surfaces and Contact Angle Measurements. Four test surfaces were prepared using aluminum substrates. They were composed of: First, a plain surface (abbreviated as p), commonly used in fins, as part of fin-tube heat exchangers; second, a plain hydrophobic surface (p-hp), prepared by functionalization of the r surface with 1H, 1H, 2H, 2H-perfluorodecyltriethoxysilane (PDES); third, a superhydrophilic aluminum surface (h), comprising the hierarchy discussed in the previous section and fourth, a hydrophobic aluminum surface comprising the hierarchical structures (h-hp), prepared by functionalization of the h surface with PDES (Scheme 1). Table 1 presents the static, advancing and receding contact angles, and contact angle hysteresis (CAH) of the test surfaces.

Table 1. Contact Angle Data of the Test Surfaces

surface	static contact angle θ (deg)	advancing contact angle θ_A (deg)	receding contact angle θ_R (deg)	CAH = $\theta_A - \theta_R$ (deg)
plain (p)	71.1 ± 1.7	98.9 ± 1.5	67.7 ± 1.6	31.2
plain-hydrophobic (p-hp)	97.2 ± 1 0.0	113.2 ± 1.0	95.2 ± 0.9	18
hierarchical (h)	<5	<5		
hierarchical-hydrophobic (h-hp)	148.8 ± 2.2	157.8 ± 0.8	134.5 ± 6.5	6.6

Table 1 shows that p is moderately hydrophilic (θ = 71.1°). Silane functionalization of p renders the surface slightly hydrophobic, which is presented as p-hp (θ = 97.2°). The hierarchically structured surface, h, shows a superhydrophilic nature (θ < 5°), whereas upon functionalization, h-hp shows hydrophobic character (θ = 143.7°). The h surface was superhydrophilic and absorbed droplets through capillary action as soon as they came into contact with the surface. Therefore, receding angle and CAH could not be measured for this surface. The CAH values of the surfaces and their relation to the latent heat transfer coefficient and water harvesting behavior will be discussed in the later sections.

Shedding Mechanisms vs Subcooling. To observe and compare the shedding mechanisms of droplets on the test surfaces as a function of subcooling, we recorded droplet dynamics during condensation using the same configuration as shown in Figure 1e.

Representing a conventional heat exchanger fin surface, p exhibited irregularly shaped droplets of the order of 1 mm on its surface, across the entire range of subcooling (Figure 2a). These millimeter-sized droplets continue to coalesce with the freshly nucleating smaller droplets in their vicinity and grow bigger in size (Figure S5). However, they only shed from the surface after reaching a size on the order of 1 mm. Surface coverage by such droplets reduces the available area for fresh condensate to appear, thereby inhibiting heat exchange with the surroundings.

Droplets on the p-hp surface remain spherical to a greater extent than p surface, because of the lower surface energy (Figures S5 and S6). However, the droplets on the p-hp surface only shed at higher subcooling via rolling, that too upon reaching a size on the order of 1 mm. Surface h shows the presence of droplets of sizes ranging from tens to hundreds of micrometers across the entire range of subcooling. The white regions are indicative of reflectance occurring from wet spots. Figure 2c-i shows encircled wet bundles and a droplet on the order of 100 μm resting on one such bundle. The wet bundles are also shown in Video S3. Figure 2c-ii shows multiple droplets of the order of 10 μm on a single bundle, indicated by arrows. An identical droplet behavior is observed at high subcooling, with representative droplets on the order of 100 μm, shown in Figure 2c-iii. The growth and nature of shedding for droplets on the h surface are discussed in the next section.

Shedding on Hierarchical Structures. To observe the mechanism for droplets on the order of 100 μm, we recorded a video with multiple such droplets in a frame, at 30 frames per second, under full-ring illumination (Video S1). The droplets reside on top of the bundles, whereas the base of the bundles is covered with water film (Figure 3a). The droplets can therefore only reside in a Cassie−Bexter or Wenzel state, with air gaps between themselves and the basal film. They grow intermittently and undergo slight movement (for example, at t = 02:41.70 min), until the base area of the droplet grows beyond that of the bundle, resulting in toppling of the droplet down the bundle to merge with the basal film (Figure 3a and Figure S10, t = 05:17.67). The merged droplet extends itself across the base of the bundle and the surrounding film, as suggested by the distorted reflection of the illuminated ring within the droplet (Figure 3a, t = 05:17.67). This toppling-assisted coalescence, or Mode 1, is shown schematically in Figure 4a.

Another mechanism of drop-to-film coalescence for ∼100 μm droplets is observed when a drop receded into the surrounding bundle upon coming into its contact, via capillary action (Figure 3a, Mode 2, t = 3:39.75 min). This is represented as Mode 2 in the schematic shown in Figure 4a. Time-lapsed images are shown in Figure 3b.

To observe the dynamics of droplets on the order of 10 μm, we focus on a single bundle and record the dynamics at 30 frames per second (Video S2). The large droplet observed initially was pinned to the bundle and kept growing in a partial wetting (PW) state (Figure 3b, $t \leq$ 5:50.34 min), until it came in contact with the basal film at the bundle. After coalescence with the basal film, fresh droplets were seen growing and coalescing on the bundle (t = 5:50.37−06:29.12 min), which eventually combined to form a large droplet of size comparable to that of the bundle (t = 13:39.91 min). The large droplet continues to grow in the PW state until coalescence with the basal film occurs again (t = 13:39.94 min). This cycle repeats itself. Schematic representation of this cycle is shown in Figure 4b, divided into six stages.

https://dx.doi.org/10.1021/acsanm.0c03032
ACS Appl. Nano Mater. 2021, 4, 1540−1550

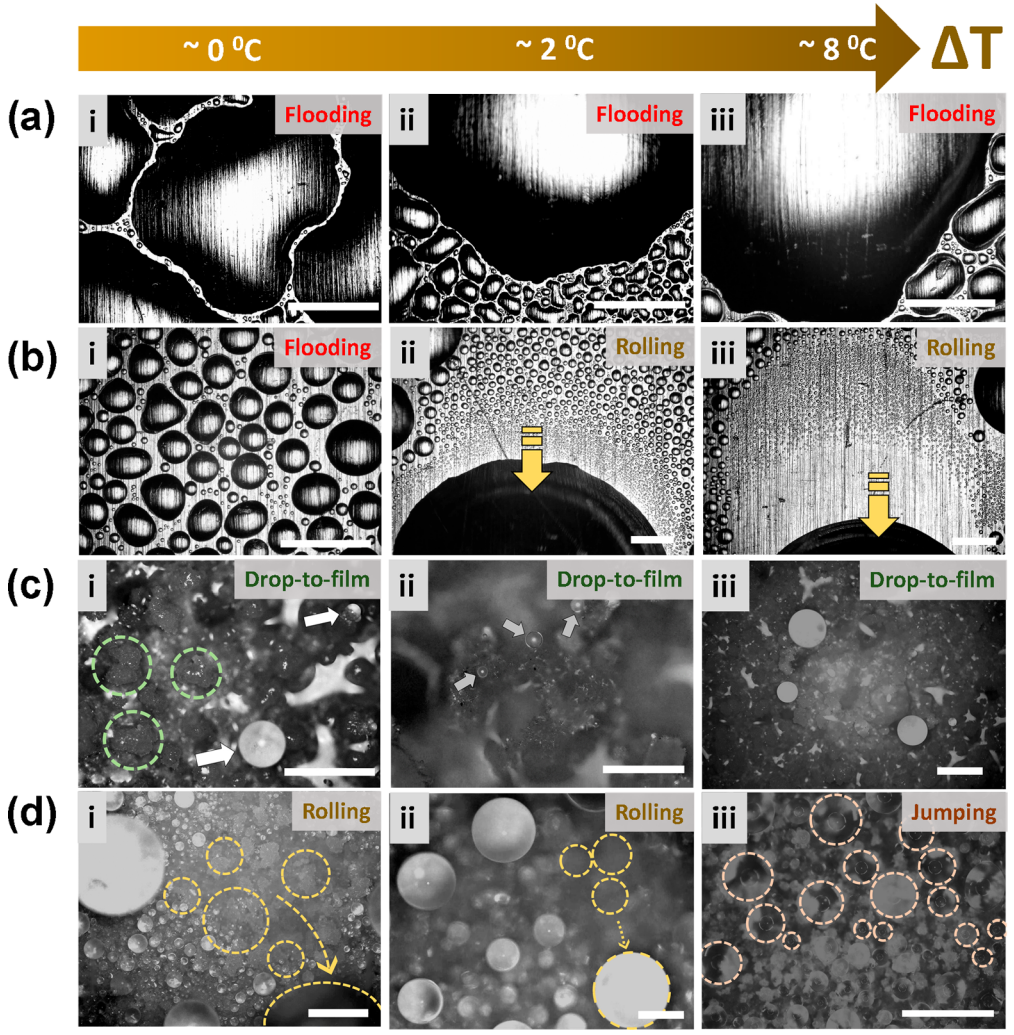

Figure 2. Optical images showing shedding mechanisms on test surfaces at varying degrees of subcooling. The observations were begun only after 30 min of condensation had already happened and condensation dynamics had stabilized. (a) Pain aluminum surface, p. Scale bar: 1 mm. (b) Plain-hydrophobic surface, p-hp. Scale bar: 1 mm. (c) Hierarchically structured surface, h. Dashed circles in i indicate reminiscent wet bundles, after the respective droplets have undergone coalescence with the film (Figure S7). The white arrows in i and ii indicate droplets on different bundles and on the same bundle, respectively. Scale bar: 500 μm. (d) Hierarchically structured hydrophobic surface, h-hp. The dashed yellow circles in i and ii represent regions where droplets were present a few milliseconds (ms) ago and are removed now, after coalescence and subsequent rolling (Figure S8). The dashed pink circles in iii represent regions where previously present droplets combined and jumped-off the surface, resulting in the present image. Scale bar: 500 μm.

Given the presence of basal film across the entire surface, parts of the surface has completely submerged bundles (Figure 4c), which become visible only upon drying using a hot air blower (Video S3). Therefore, observed droplets could nucleate only on bundles with heights more than the thickness of the basal film.

Because the lowering of surface energy promotes DwC on a surface and improves droplet mobility and rate of surface renewal, it becomes crucial to perform low-surface-energy functionalization of the h surface to promote DwC and understand the difference in shedding mechanisms between the h and h-hp surfaces. Moreover, although the h-hp surface has microstructures to retain Cassie−Baxter (CB) state of droplets, it also possesses nanostructures on top of these microstructures, to allow smaller droplets to nucleate beneath the CB droplet and eventually merge with it, leading to hierarchical condensation. To verify this claim, we performed dynamic optical imaging during condensation on the surface (Figure 5). Droplets on a single bundle are monitored (bundle lying within the dashed square box in Figure 4a). Initially (t = 0 min), several droplets on the order of 100 μm are found on the bundle that coalesce with time and become larger in size (t = 8 s), also moving slightly over the bundle by releasing free energy after coalescence. This renews the surface for fresh droplets to nucleate (t = 8 min 18 s), whereas the bigger droplet continues to grow through condensation as well as coalescence. Upon reaching a certain size, greater than 500 μm (t = 9 min 24 s), the bigger droplet rolls off the bundle. Thereafter, fresh droplets nucleate and grow (t = 14 min 26 s), repeating the cycle. Coalescence of droplets happening on the tip of the bundle is also assisted by the coalescence of shaded droplets, present beneath the bigger droplet (Figure 5b-i). This is proved by performing focal plane shift imaging (FPSI) on another substantially big droplet (>500 μm) on the surface (Figure 5b). Upon shifting the focal plane at an intermediate position, between the droplet base and the base of the surface, numerous smaller droplets of the order of 10 μm are seen undergoing movement and coalescence on the conical surfaces.

https://dx.doi.org/10.1021/acsanm.0c03032
ACS Appl. Nano Mater. 2021, 4, 1540−1550

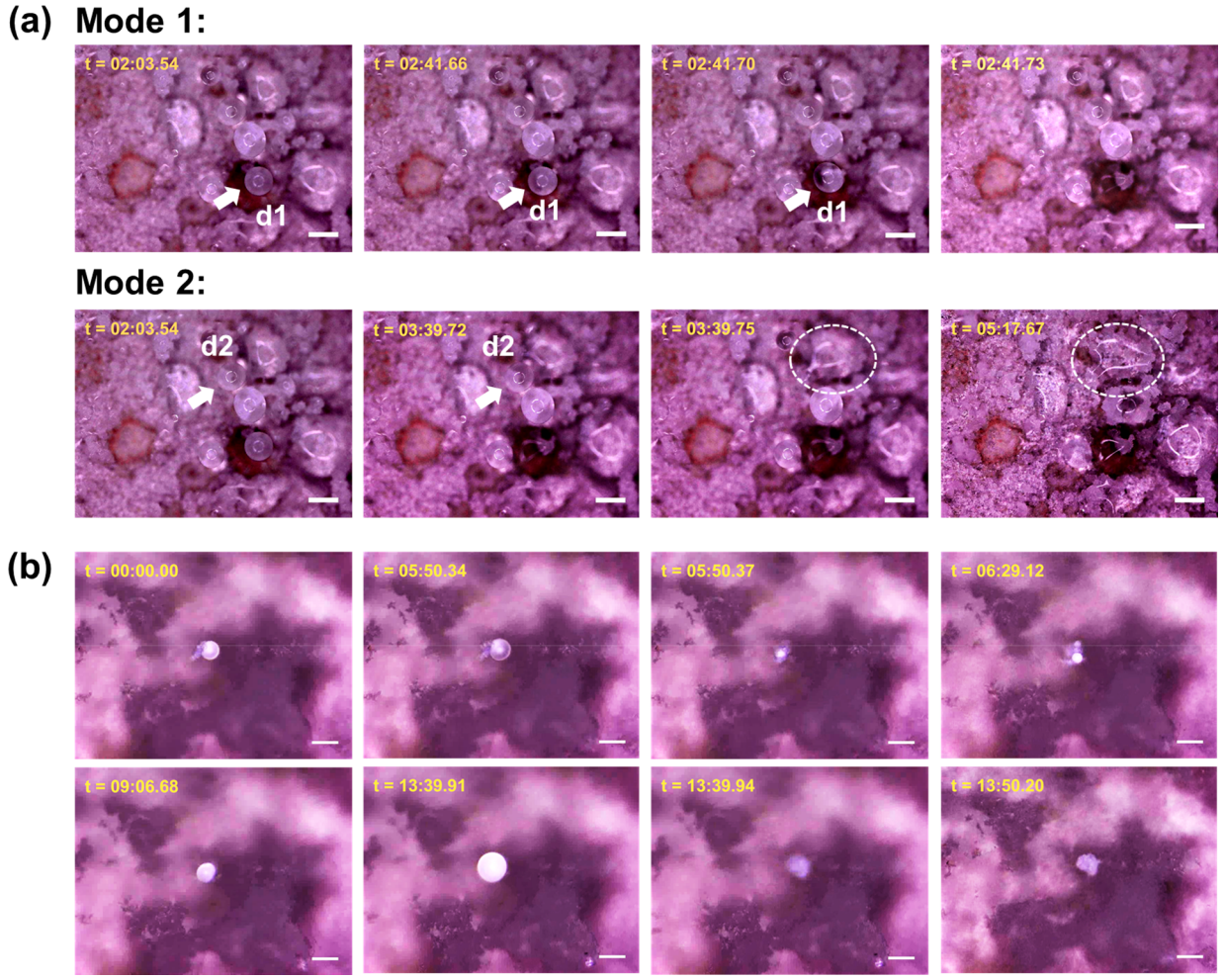

Figure 3. Drop-to-film condensation. (a) Mode 1 and Mode 2 are shown using select droplets of the order of 100 μm, undergoing drop-to-film condensation. Mode 1 shows toppling-induced coalescence occurring at t = 2:41.73 min, where a droplet topples from the bundle upon reaching a critical size. Mode 2 shows capillary-induced coalescence where droplet d2 recedes into the film via a neighboring bundle that acts as a capillary. Scale bar: 100 μm. (b) Dynamics of droplets on the order of 10 μm on a single bundle. A droplet grows on the bundle and coalesces at t = 5:50.37 min, followed by nucleation of new droplets that combine to form a larger droplet on the bundle, which grows until it encounters the film underneath and coalesces with the film. Scale bar: 50 μm.

As an illustration, Figure 4b-ii, iii shows shaded droplets 1 and 2 undergoing coalescence and resulting in 1′, whereas droplet 3 lost its sphericity and hung between the cones as 3′. The presence of shaded droplets like 1, 2, 3, 1′, and 3′ beneath the larger droplet shown in Figure 5b-i confirms hierarchical condensation, also reported previously by Yan et al.[14] In combination with hierarchical condensation, cross-sectional imaging of the surface at high subcooling (~8 °C) also reveals the jumping-droplet mode of shedding (see Figure S9). However, the jumping mode is not observed at lower subcooling.

Heat Transfer Performance. After developing an understanding of the shedding phenomena for the test surfaces, we further test the surfaces for their water harvesting performances and the corresponding latent (or condensation) heat transfer coefficients, by exposing them to a constant ambient air flux at varying amounts of subcooling (see Methods). Figure 6a represents a schematic of the setup wherein a test surface is placed on a Peltier-heat sink assembly and cooled down to the required temperature by supplying DC power to the Peltier. A constant ambient air flux is maintained over the surface using a DC fan (see Methods). Each collection experiment is performed for 3 h. It is noteworthy that unlike a majority of the previous studies,[19−22] in which condensation is performed by exposing the surface to saturated humidity in a closed chamber, we perform all lab-scale experiments in the presence of noncondensable gases. The water collection flux, as plotted in Figure 6b, shows substantially better performance of the h surface, compared to the other surfaces, particularly in the subcooling regime of ~1−6 °C. Regardless of the degree of subcooling, the h surface begins to collect water 30−50 min after the beginning of the experiment, whereas others followed a sharp increase in the collection onset with a decrease in subcooling (Figure 6c). We further evaluate the latent heat transfer coefficient, HTC, using the following equation:

$$\mathrm{HTC} = \frac{\dot{m} h_{\mathrm{fg}}}{\Delta T} \tag{1}$$

where $\dot{m}$ is the mass transfer flux, or the rate of water collection.[23] The HTCs for different subcooling were plotted separately, to highlight the differences at each subcooling.

Postnucleation, when a droplet reaches a critical size during its growth after multiple coalescence events, the gravitational force exerted by the droplet balances the retention force,

https://dx.doi.org/10.1021/acsanm.0c03032
ACS Appl. Nano Mater. 2021, 4, 1540−1550

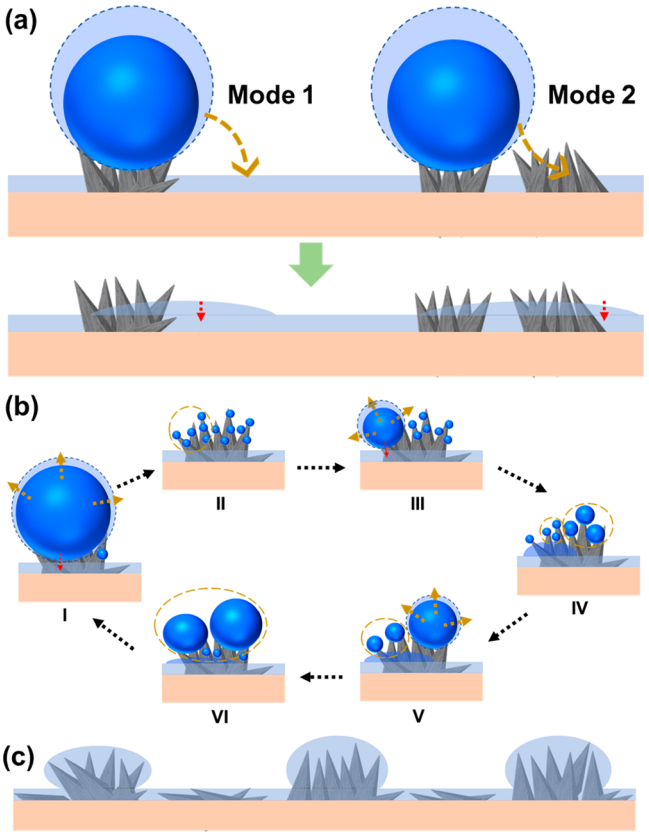

Figure 4. Configurations of water present on the h surface. (a) Droplet on the order of 100 μm rolls down the bundle upon crossing the bundle size at its base (Mode 1). Another droplet (Mode 2) on the same order recedes into the basal film through a neighboring bundle upon coming into its contact, via capillary action. (b) Large droplet, a few tens of micrometers in size, undergoes coalescence with the film beneath it (Stage I). This is followed by the growth of fresh droplets on multiple cones (Stage II), which coalesce with each other, and the bigger droplet continues to grow in a partial wetting state (Stage III) until it comes into contact with the basal film to subsequently get drained. This allows fresh nucleation (Stage IV) and subsequent coalescence (Stage V and VI), and the process continues in a cycle (Video S2). (c) Bundles completely covered with water (Video S3).

causing it to roll down the surface. The critical size can be obtained from the following equation:

$$mg\sin\alpha = \gamma_{water}(\cos\theta_a - \cos\theta_r)W \quad (2)$$

where expression on the left side of the equation represents the gravitational force exerted by the droplet of mass m, parallel to the surface with tilt angle α, γ_{water} is the surface tension of water, θ_a and θ_r are the advancing and receding angles, respectively, and W is the width of the droplet.[24] Therefore, lower CAH ($\theta_a - \theta_r$) implies lower droplet critical size, which should contribute to a faster rate of surface renewal and therefore lead to better water collection or mass transfer. Figure 6c shows that droplets begin to roll earlier on a surface with lower CAH as the collection on r-hp begins earlier compared to p, at all degrees of subcooling. When cumulative water collection for 3 h is plotted against subcooling, it is observed that at low and intermediate subcooling (<3 °C), r-hp is a better collector compared to r. Lower CAH in the case of p-hp leads to higher mobility of the droplets, allowing them to roll down easily. At high subcooling (>6 °C), p provides better collection flux than p-hp, indicating that affinity for water vapor, or rate of nucleation, dominates over CAH in this regime. Surface functionalization for planar surfaces, therefore, limits the collection flux and HTC at high subcooling but improves both at low subcooling.

The h surface showed the highest HTC across the entire subcooling range. When compared to the p surface, the h surface demonstrated as high as a 10-fold improvement (~1048.4%) in HTC at $\Delta T \approx 1$ °C. The superior performance of h is attributed to the presence of a large number of nucleation sites, the dual nature of nanochannels that allows effective drop-to-film coalescence, and the presence of faceted microcones all across the base, which greatly reduces the basal area occupied by the film, thus preventing domination of the film mode of condensation. Given the complex morphology of h and h-hp, wetting states of the droplets, and their coalescence mechanisms, functionalization does not provide a clear overall advantage in terms of collection flux (or HTC). Although h always shows better overall performance compared to h-hp, the difference is more significant at low subcooling. The poor performance of h-hp at low subcooling can be attributed to its lower affinity toward water vapor, resulting in a lower rate of nucleation. This factor becomes insignificant at high subcooling and the difference between h and h-hp is reduced with an increase in subcooling, mainly due to hierarchical condensation occurring on the h-hp surface, which eliminates the possibility of flooding at high subcooling. Also, hierarchical condensation is supported by the jumping-droplet mode on h-hp, which occurs only at high subcooling. Therefore, nanochannel-assisted drop-to-film coalescence proves to be the most efficient mode of condensation, among other existing modes, such as jumping-droplet condensation,[3,25−27] FwC, DwC,[6,28,29] hierarchical condensation,[14] and a combination of jumping-droplet and hierarchical condensation mechanisms. However, the observed enhancement in HTC obtained in the case of the h surface, at lab-scale, should be retained while performing large-scale condensation as well, such as on tube-fin heat exchangers, where practical challenges like local water logging between the fins or complex surface−air interaction due to compact arrangement of fins may reduce the heat transfer and, rather, bring down the collection efficiency. Therefore, two refrigeration-based AWG prototypes are assembled in which the evaporators comprise p and h surfaces to verify whether improved HTC at lab-scale, in the case of h surface, translates to enhanced collection efficiency of its corresponding prototype at an industry scale. The following section discusses the details about assembled prototypes, their testing, and results.

Feasibility of h-Surface after Scale-up. A home-build AWG prototype of 25 L/day capacity (Figure 7a and Figure S11) is assembled, which comprises a standard refrigeration cycle to cool the h surface below the dew point. Two identical prototypes are created, where the evaporator in one comprises fins made of the conventional p surface (the p prototype), and the other comprises fins made of the h surface (the h prototype). Therefore, the only difference between the two prototypes is the surface morphology of the evaporator fins. The collected water is filtered and mineralized to render it drinkable. However, the aspect of quality of the collected water is deliberately not discussed, to avoid deviation from the focus of this article.

The prototypes were kept in the open and run for ~4 h in the evening (3:24−7:24 p.m.) on March 6, 2020, in Chennai,

https://dx.doi.org/10.1021/acsanm.0c03032
ACS Appl. Nano Mater. 2021, 4, 1540−1550

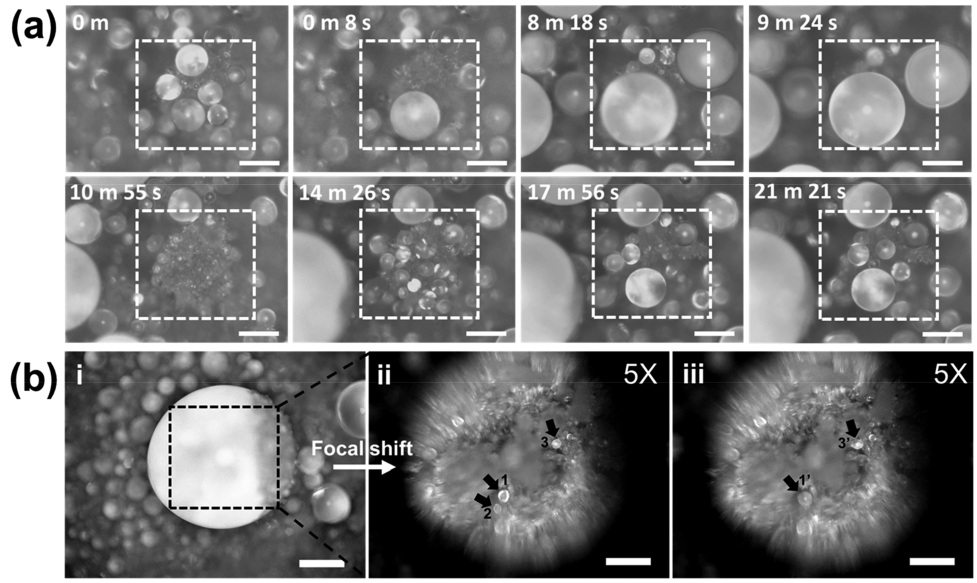

Figure 5. Dynamic optical imaging of h-hp surface during condensation. (a) Top view of the surface, showing droplet dynamics on a single bundle confined within the dashed white box. Scale bar: 200 μm. (b) (i) Larger sink droplet. Scale bar: 500 μm. (ii) Upon shifting the focal plane beneath the droplet, in the dashed black box region, shaded droplets are observed that undergo coalescence (1 + 2 = 1′) and distortion in shape (from 3 to 3′) during movement across microcones, as shown in (iii). Scale bar: 500 μm.

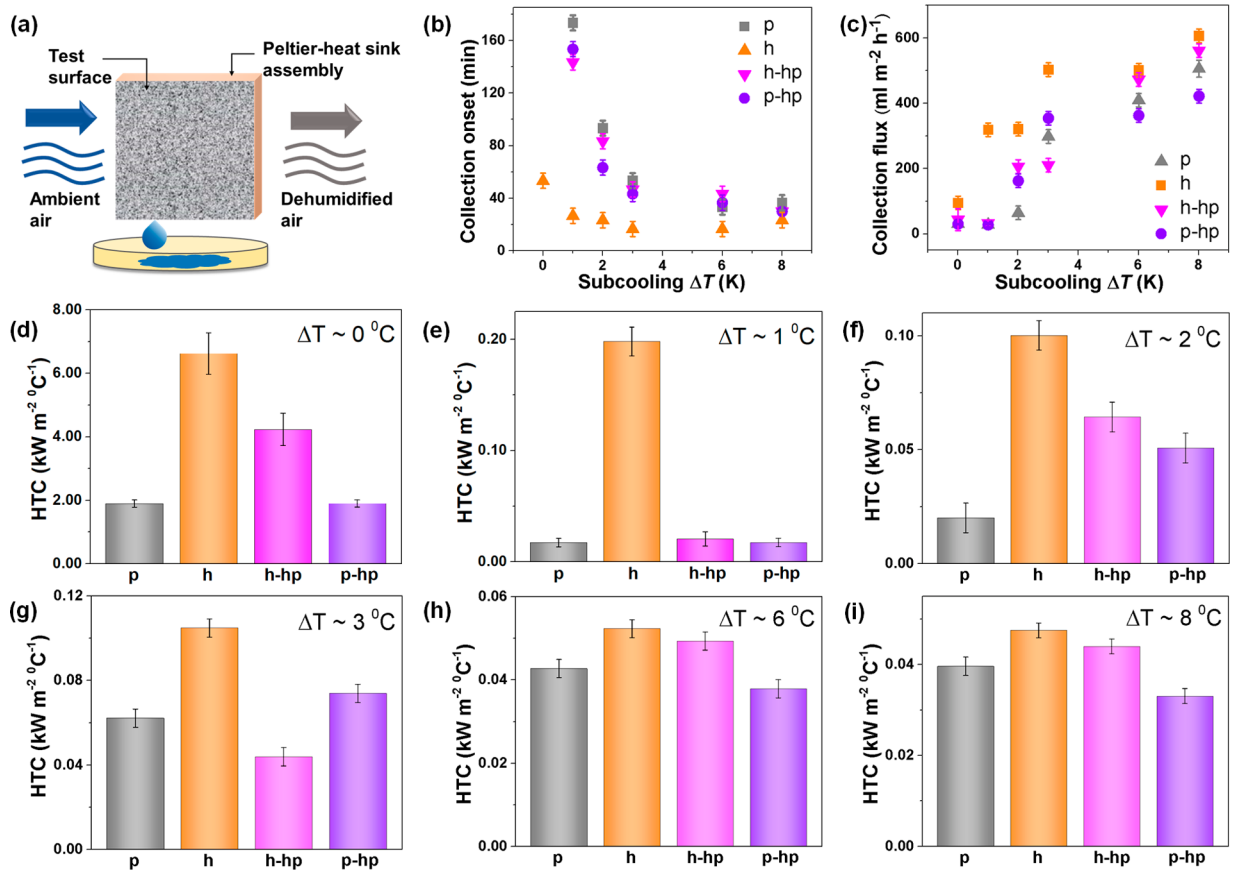

Figure 6. (a) Schematic of the setup for testing water collection performance of the test surfaces. (b) Plot of onset of water collection against subcooling. (c) Cumulative water collected plotted as water collection flux against subcooling. (d–i) Latent heat transfer coefficients for all test surfaces corresponding to water collection experiments performed on the test surfaces across the subcooling range of ~0–8 °C.

India. Five trial runs are performed (Figure 7 and Figures S12–S16). The temperature during the test run dropped from 38.7 to 30 °C, whereas RH increased from 44 to 67% (Figure 7b). As a result, the dew point dropped from 27.5 to 23.4 °C (Figure S8b). During the course of the test run, the h surface showed an ~10.8% enhancement in the overall water collection, and an ~10.4% improvement in the average collection efficiency, compared to the p surface (Figure S8a

https://dx.doi.org/10.1021/acsanm.0c03032
ACS Appl. Nano Mater. 2021, 4, 1540–1550

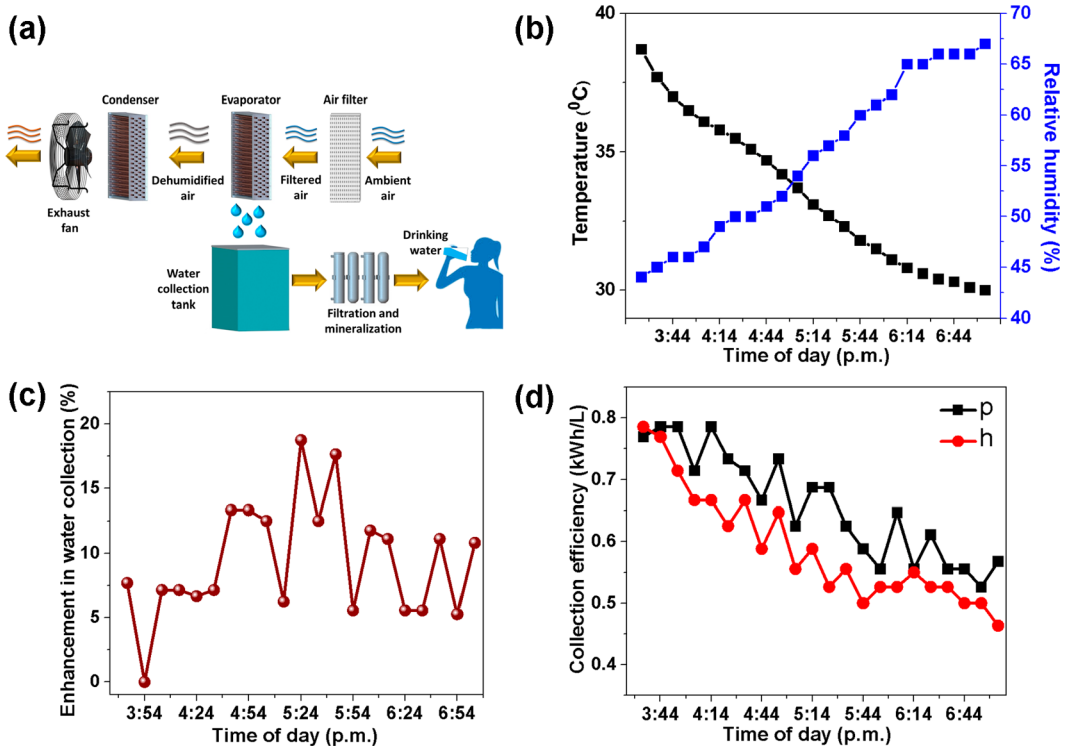

Figure 7. Prototype testing corresponding to h and p surfaces. (a) Schematic of the AWG prototype of 25 L/day capacity, where evaporator fins were the only difference between the two prototypes. (b) Ambient conditions (temperature and RH) during the course of testing. (c) Percentage enhancement in water collection of the h prototype compared to the p prototype as a function of time. (d) Collection efficiency of the prototypes as a function of time.

Table 2. Commercial Refrigeration Cycle-Based Water Generators Worldwide

			Ambient conditions		
organization	power consumption (W)	rRate of water production (L day^{-1})	T (°C)	relative humidity (%)	collection efficiency (kWh/L)
H2O machine (USA)[30]	1700	68			0.60
GENAQ Technologies (Spain)[31]	700	50			0.34
Atlantis Solar and Wind (USA)[31]	1200	100			0.29
Atmos H2O (USA)[32]	500	23			0.52
Airowater (India)[33]	500	25		70	0.48
Nu Image Solutions (USA)[34]	830	30	30	80	0.66
Ray Agua (Spain)[35]	2450	200	30	80	0.35
WAE (India)[36]	400	50			0.91
Hendrx Water (China)[37]	900	15	30	80	1.44
this work (h prototype)	656	25	33	56	0.63

and Figure 7d). The percentage enhancement in the collection performance of the h prototype, compared to the r prototype, ranged from 0 to 17.6% across the duration of the experiment (Figure 7c). The collection efficiency of the prototypes is compared by plotting the amount of energy consumed per liter of water produced. Considering all the energy-consuming parts (except postcollection processes) of the prototypes, the h prototype was consistently more energy efficient than the p prototype during the course of testing (Figure 7d). Such behavior is observed across almost all trial runs (Figures S12–S16). The advantage of energy savings due to a drop-to-filmwise shedding mechanism could be further leveraged by periodically turning the power off briefly before the replenishment is about to occur and turning it on immediately after the it is complete. This will lead to energy-efficient shedding and eliminate the local maxima in the h-curve (Figure 7d). Adopting such a strategy for the r surface will not offer a significant advantage because of absence of any "sharp-curvature" nucleation sites for quick nucleation of fresh droplets, postshedding, when the power is turned on again. Faster drop-to-filmwise shedding may be another way forward by mechanical agitation once the droplets have been nucleated.

Several commercial water generators based on refrigeration cycle-based active cooling are available. The performance of these systems depends on the ambient temperature, relative humidity, absolute humidity, air flux across the condensing surface, amount of refrigerant, and system design. Given these dependencies, an exact comparison is not possible. Nevertheless, we list out nine water generators across the globe alongside our prototype to provide a fair idea of the value of this work (Table 2).

https://dx.doi.org/10.1021/acsanm.0c03032
ACS Appl. Nano Mater. 2021, 4, 1540−1550

CONCLUSIONS

For efficient and scalable heterogeneous condensation, we propose a hierarchically textured surface, fabricated by a one-step process, exhibiting drop-to-film condensation. The surface exhibits a higher heat transfer coefficient compared to its functionalized counterpart, and the conventional plain metal surfaces used as references, which show dropwise, film-wise, jumping-droplet, or hierarchical condensation. The drop-to-film coalescence on the hierarchical surface occurs via nanochannels. Following are the primary reasons for the enhanced heat transfer obtained in case of hierarchical surface: (1) the large number of nucleation sites offered by the faceted microcones and the nanostructures present on their surfaces; (2) high affinity for water vapor; and (3) capillary-action assisted, or toppling-induced coalescence of droplets on the order of 100 μm with the basal film. These advantages have led us to a significant 10.8% improvement in the overall water collection of the prototype composed of hierarchical condensing surface, compared to a prototype containing a plain metal condensing surface, whereas the instantaneous improvement (over a 10 min period) in collection ranged from 0 to 17.6%, depending on the atmospheric conditions during field testing. The above-mentioned reasons together with the strategy of further enhancing energy efficiency by ways such as periodic supply of power, better heat exchanger design, induction of mechanical vibrations for faster shedding, etc., will further render the surface fit for scalable use in applications ranging from water generation to heat management.

METHODS

Fabrication of the Test Surfaces. The dual-nanostructured hierarchical surface (h) was fabricated by dipping the plain surface in NaOH solution (30 mM) prepared in deionized (di) water for a period of 15 h at a temperature of 60 °C. The surface was subsequently rinsed in di water and dried with a hot air gun.

The functionalized surfaces, r-hp and h-hp, were prepared by dipping the p and h surfaces in 1% ethanol solution of PDES for a period of 2 h. The surfaces were subsequently taken out, rinsed in deionized water, and dried using an air gun.

Contact Angle Measurements. Contact angle measurements were performed using drops of volume ~3 μL using a Holmarc contact angle meter.

Surface Characterization. Morphology of the hierarchical surface was observed using scanning electron microscope (Verios G4 UC, FEI) and optical microscope (VH-Z100R, Keyence).

For powder X-ray Diffraction (XRD), the h surface was scraped and powder was collected. The measurement was performed on Bruker D8 Advance X-ray powder diffractometer. The plot of diffraction intensity vs 2θ revealed presence of $Al_2O_3{\cdot}3H_2O$ and $Al(OH)_3$ phases, belonging to hexagonal and monoclinic crystal systems, respectively (Figure S1).

Topography and roughness were obtained by performing atomic force microscopy on the as-prepared surface using a Witec GmbH confocal Raman microscope (CRM-Alpha300 S) in a region of 10 μm × 10 μm.

The uniform functionalization of the h-hp and p-hp surfaces is evident from the EDS mapping performed on both surfaces and distribution of fluorine in them (Figure S2, S3).

Observation of Shedding Mechanisms. We chose low (~0 °C), intermediate (~4 °C), and high (~8 °C) subcooling conditions for this study. All laboratory experiments were performed at ambient conditions at a temperature of 23.6 ± 0.5 °C and relative humidity of 50 ± 1% in still air. The test surface (4 cm × 4 cm) was adhered to the cold side of a Peltier using silver paste. The Peltier was then anchored on a heat sink DC fan assembly using the same silver paste. The Peltier was then connected to a DC power supply to calibrate input power as a function of surface temperature. The video recording was begun only after ~30 min of condensation had already taken place and the dynamics had reached an equilibrium. Videos were recorded for each surface and each selected subcooling value, and key frames represented in Figure 2 were selected from the videos. During each recording, the magnification was varied from 100× to 1000×, and droplets across the entire surface were observed to identify their variety. We have made a reasonable assumption that wetting states of droplets, the nature of coalescence events, and shedding modes are independent of air flux across the surface. Therefore, all imaging experiments were performed in still air to avoid noise because of air flow and concerned regions were kept under focus.

Shedding on Hierarchical Structures. The droplet dynamics were investigated under an optical microscope in the same configuration as shown in Figure 1b. The hierarchical surface temperature was kept at the dew point (12.6 °C; under ambient conditions of 23.6 °C, 50% RH).

FPSI on h-hp Surface. To verify the hierarchical mode of condensation and capture droplet dynamics on a single bundle, we kept a single bundle under focus and recorded a video. Imaging was begun only after 30 min of condensation had occurred (at $\Delta T \approx 0$ °C) and the droplet dynamics had stabilized. For FPSI, a bigger droplet was focused and the focal plane was gradually shifted from the top surface of the droplet to beneath it. This brought the smaller droplets into focus, that existed beneath this large droplet.

Heat Transfer Experiments. A square duct with the duct size of 4 cm × 4 cm was created and the Peltier-heat sink assembly was fitted inside the duct in a way that only the surface protruded on the inside wall of the duct, parallel to it (Figure S4). A DC fan flowing ambient air at a constant speed on 2.5 m/s (or a flux of 8.65 cubic feet per minute) across the duct was put at one end, leaving the other end open for dehumidified air to exit. Along with the hierarchical surface, we select test surfaces such that all modes of condensation could be observed, either individually, or in combination with one another, for comparison of their performance under identical conditions.

Fabrication of the Prototypes. For the h prototype, the rolled sheet of aluminum (0.1 mm in thickness) was kept for etching in a 30 mM NaOH solution, prepared in di water. Fins of the size 10 in. × 14 in. were prepared out of the etched sheet and a punching die was used to create holes for fitting the copper tubes. The fins were packed in the traditional fin-tube heat exchanger configuration with a density of 12 fins per inch, resulting in a combined surface area of 4.07 m^2. This assembly was used as the evaporator. Further, another identical heat exchanger was prepared, but with the unetched sheet, to be used as condenser. An AC fan (22A230HBAC) was used to provide an air flux of 360 cubic feet per minute across the system.

The p prototype was identical to the h prototype, except that the evaporator and condenser both comprised unetched fins in the case of p prototype.

Test Runs of the Prototypes. Five test runs with variable time intervals were performed on the two prototypes during day time in Chennai, India. During each test run, ambient conditions (temperature and RH), surface temperature of the fins, and water collected were measured in intervals of 10 min.

ASSOCIATED CONTENT

Supporting Information

The Supporting Information is available free of charge at https://pubs.acs.org/doi/10.1021/acsanm.0c03032.

Powder XRD and SEM-EDS, lab-scale prototype, optical images of jumping-droplet condensation on the hierarchical superhydrophobic surface, images of the scaled prototype, and results of test runs of prototypes (PDF)

Video S1, video of multiple 100 μm droplets in a frame, at 30 frames per second, under full-ring illumination (MP4)

https://dx.doi.org/10.1021/acsanm.0c03032
ACS Appl. Nano Mater. 2021, 4, 1540−1550

Video S2, dynamics of droplets of the order of 10 μm on a single bundle at 30 frames per second (MP4)
Video S3, drying of wet bundles using hot air flow (MP4)

AUTHOR INFORMATION

Corresponding Authors

Tiju Thomas − *Department of Metallurgical and Materials Engineering, Indian Institute of Technology Madras, Chennai 600036, India;* orcid.org/0000-0001-8322-6387; Email: tijuthomas@iitm.ac.in

Thalappil Pradeep − *DST Unit of Nanoscience, Thematic Unit of Excellence, Department of Chemistry, Indian Institute of Technology Madras, Chennai 600036, India;* orcid.org/0000-0003-3174-534X; Email: pradeep@iitm.ac.in

Authors

Ankit Nagar − *DST Unit of Nanoscience, Thematic Unit of Excellence, Department of Chemistry and Department of Metallurgical and Materials Engineering, Indian Institute of Technology Madras, Chennai 600036, India*

Ramesh Kumar − *Department of Metallurgical and Materials Engineering, Indian Institute of Technology Madras, Chennai 600036, India*

Pillalamarri Srikrishnarka − *DST Unit of Nanoscience, Thematic Unit of Excellence, Department of Chemistry, Indian Institute of Technology Madras, Chennai 600036, India;* orcid.org/0000-0001-5187-6879

Complete contact information is available at: https://pubs.acs.org/10.1021/acsanm.0c03032

Notes

The authors declare no competing financial interest.

ACKNOWLEDGMENTS

We gratefully acknowledge the Department of Science and Technology (DST) for supporting our research program. A.N., P.S., and C.S. thank IIT Madras for their doctoral student fellowships. We also acknowledge the help offered by Sagar Patil, Sudeep Patel, Guthi Raja, Swathi Choudhary, and Arpan Soren during prototype assembly and testing.

REFERENCES

(1) Nagar, A.; Pradeep, T. Clean Water through Nanotechnology: Needs, Gaps, and Fulfillment. *ACS Nano* **2020**, *14* (6), 6420−6435.
(2) Dulberg, S.; Kohavi, A. System and Method for High-Efficiency Atmospheric Water Generator and Dehumidification Apparatus. U.S. Patent 20180266708, 2018.
(3) Miljkovic, N.; Enright, R.; Nam, Y.; Lopez, K.; Dou, N.; Sack, J.; Wang, E. N. Jumping-Droplet-Enhanced Condensation on Scalable Superhydrophobic Nanostructured Surfaces. *Nano Lett.* **2013**, *13* (1), 179−187.
(4) Tu, R.; Hwang, Y. Reviews of Atmospheric Water Harvesting Technologies. *Energy* **2020**, *201*, 117630.
(5) Tu, Y.; Wang, R.; Zhang, Y.; Wang, J. Progress and Expectation of Atmospheric Water Harvesting. *Joule* **2018**, *2* (8), 1452−1475.
(6) Parin, R.; Martucci, A.; Sturaro, M.; Bortolin, S.; Bersani, M.; Carraro, F.; Del Col, D. Nano-Structured Aluminum Surfaces for Dropwise Condensation. *Surf. Coat. Technol.* **2018**, *348*, 1−12.
(7) Maa, J. R. Drop Size Distribution and Heat Flux of Dropwise Condensation. *Chem. Eng. J.* **1978**, *16* (3), 171−176.
(8) Orejon, D.; Askounis, A.; Takata, Y.; Attinger, D. Dropwise Condensation on Multiscale Bioinspired Metallic Surfaces with Nanofeatures. *ACS Appl. Mater. Interfaces* **2019**, *11* (27), 24735−24750.
(9) Rose, J. W. Dropwise Condensation Theory and Experiment: A Review. *Proc. Inst. Mech. Eng., Part A* **2002**, *216* (2), 115−128.
(10) Chen, X.; Wu, J.; Ma, R.; Hua, M.; Koratkar, N.; Yao, S.; Wang, Z. Nanograssed Micropyramidal Architectures for Continuous Dropwise Condensation. *Adv. Funct. Mater.* **2011**, *21* (24), 4617−4623.
(11) Oh, J.; Zhang, R.; Shetty, P. P.; Krogstad, J. A.; Braun, P. V.; Miljkovic, N. Thin Film Condensation on Nanostructured Surfaces. *Adv. Funct. Mater.* **2018**, *28* (16), 1707000.
(12) Edalatpour, M.; Liu, L.; Jacobi, A. M.; Eid, K. F.; Sommers, A. D. Managing Water on Heat Transfer Surfaces: A Critical Review of Techniques to Modify Surface Wettability for Applications with Condensation or Evaporation. *Appl. Energy* **2018**, *222*, 967−992.
(13) Hou, Y.; Yu, M.; Chen, X.; Wang, Z.; Yao, S. Recurrent Filmwise and Dropwise Condensation on a Beetle Mimetic Surface. *ACS Nano* **2015**, *9* (1), 71−81.
(14) Yan, X.; Chen, F.; Sett, S.; Chavan, S.; Li, H.; Feng, L.; Li, L.; Zhao, F.; Zhao, C.; Huang, Z.; Miljkovic, N. Hierarchical Condensation. *ACS Nano* **2019**, *13* (7), 8169−8184.
(15) Yang, K.-S.; Lin, K.-H.; Tu, C.-W.; He, Y.-Z.; Wang, C.-C. Experimental Investigation of Moist Air Condensation on Hydrophilic, Hydrophobic, Superhydrophilic, and Hybrid Hydrophobic-Hydrophilic Surfaces. *Int. J. Heat Mass Transfer* **2017**, *115*, 1032−1041.
(16) Park, K.-C.; Kim, P.; Grinthal, A.; He, N.; Fox, D.; Weaver, J. C.; Aizenberg, J. Condensation on Slippery Asymmetric Bumps. *Nature* **2016**, *531* (7592), 78−82.
(17) Moazzam, P.; Tavassoli, H.; Razmjou, A.; Warkiani, M. E.; Asadnia, M. Mist Harvesting Using Bioinspired Polydopamine Coating and Microfabrication Technology. *Desalination* **2018**, *429*, 111−118.
(18) Wang, X.; Zeng, J.; Li, J.; Yu, X.; Wang, Z.; Zhang, Y. Beetle and Cactus-Inspired Surface Endows Continuous and Directional Droplet Jumping for Efficient Water Harvesting. *J. Mater. Chem. A* **2021**, *9*, 1507−1516.
(19) Cho, H. J.; Preston, D. J.; Zhu, Y.; Wang, E. N. Nanoengineered Materials for Liquid−Vapour Phase-Change Heat Transfer. *Nat. Rev. Mater.* **2017**, *2* (2), 1−17.
(20) Tsuchiya, H.; Tenjimbayashi, M.; Moriya, T.; Yoshikawa, R.; Sasaki, K.; Togasawa, R.; Yamazaki, T.; Manabe, K.; Shiratori, S. Liquid-Infused Smooth Surface for Improved Condensation Heat Transfer. *Langmuir* **2017**, *33* (36), 8950−8960.
(21) Azimi, G.; Dhiman, R.; Kwon, H.-M.; Paxson, A. T.; Varanasi, K. K. Hydrophobicity of Rare-Earth Oxide Ceramics. *Nat. Mater.* **2013**, *12* (4), 315−320.
(22) Preston, D. J.; Mafra, D. L.; Miljkovic, N.; Kong, J.; Wang, E. N. Scalable Graphene Coatings for Enhanced Condensation Heat Transfer. *Nano Lett.* **2015**, *15* (5), 2902−2909.
(23) Bergman, T. L.; Incropera, F. P.; DeWitt, D. P.; Lavine, A. S. *Fundamentals of Heat and Mass Transfer*; John Wiley & Sons, 2011.
(24) Furmidge, C. G. L. Studies at Phase Interfaces. I. The Sliding of Liquid Drops on Solid Surfaces and a Theory for Spray Retention. *J. Colloid Sci.* **1962**, *17* (4), 309−324.
(25) Mulroe, M. D.; Srijanto, B. R.; Ahmadi, S. F.; Collier, C. P.; Boreyko, J. B. Tuning Superhydrophobic Nanostructures to Enhance Jumping-Droplet Condensation. *ACS Nano* **2017**, *11* (8), 8499−8510.
(26) Kim, M.-K.; Cha, H.; Birbarah, P.; Chavan, S.; Zhong, C.; Xu, Y.; Miljkovic, N. Enhanced Jumping-Droplet Departure. *Langmuir* **2015**, *31* (49), 13452−13466.
(27) Boreyko, J. B.; Chen, C.-H. Self-Propelled Dropwise Condensate on Superhydrophobic Surfaces. *Phys. Rev. Lett.* **2009**, *103* (18), 184501.
(28) Zamuruyev, K. O.; Bardaweel, H. K.; Carron, C. J.; Kenyon, N. J.; Brand, O.; Delplanque, J.-P.; Davis, C. E. Continuous Droplet Removal upon Dropwise Condensation of Humid Air on a

Hydrophobic Micropatterned Surface. *Langmuir* **2014**, *30* (33), 10133−10142.
(29) Chen, C.-H.; Cai, Q.; Tsai, C.; Chen, C.-L.; Xiong, G.; Yu, Y.; Ren, Z. Dropwise Condensation on Superhydrophobic Surfaces with Two-Tier Roughness. *Appl. Phys. Lett.* **2007**, *90* (17), 173108.
(30) H2O Machine https://h2omachine.com/wp-content/uploads/2020/02/large-h20-spec-sheet3.pdf (accessed 2020-12-27).
(31) GENAQ Cumulus http://www.genaq.com/cumulus-tech-specs/ (accessed 2020-12-20).
(32) Atmos H2O Hawaii http://atmosh2ohawaii.com/technical-information/ (accessed 2020-12-20).
(33) AirOWater https://www.airowater.com/products/product/dewpoint/ (accessed 2020-12-20).
(34) Nu Image Solutions https://nuimagesolution.com/awg/nu-water-30.pdf (accessed 2020-12-20).
(35) Ray Agua https://www.rayagua.com/brouchers/1.CORPORATE_BROCHURE.pdfhttps://www.rayagua.com/brouchers/1.CORPORATE_BROCHURE.pdfhttps://www.rayagua.com/brouchers/1.CORPORATE_BROCHURE.pdf (accessed 2020-12-20).
(36) WAE Atmospheric Water Generator https://www.waecorp.com/emergency-equipment/36https://www.waecorp.com/emergency-equipment/36 (accessed 2020-12-20).
(37) ZL9510D Household Air Water Generator http://1909115108.pool201-site.make.yun300.cn/product/15.html (accessed 2020-12-20).

https://dx.doi.org/10.1021/acsanm.0c03032
ACS Appl. Nano Mater. 2021, 4, 1540−1550